Nanoscale

PAPER

View Article Online
View Journal | View Issue

Cite this: *Nanoscale*, 2020, **12**, 9776

Double Fano resonances in hybrid disk/rod artificial plasmonic molecules based on dipole-quadrupole coupling†

Zhiquan Chen,[a,b] Shi Zhang,[a] Yiqin Chen,[a] Yanjun Liu,[c] Ping Li,[a] Zhaolong Wang,[a] Xupeng Zhu,[d] Kaixi Bi[e] and Huigao Duan*[a]

Fano resonance can be achieved by the destructive interference between a superradiant bright mode and a subradiant dark mode. A variety of artificial plasmonic oligomers have been fabricated to generate Fano resonance for its extensive applications. However, the Fano resonance in plasmonic oligomer systems comes from the interaction of all metal particles, which greatly limits the tunability of the Fano resonance. Besides, only a single Fano resonance is supported by many existing plasmonic oligomers, while multiple Fano resonances mostly occur in complex and multilayer structures, whose fabrication is greatly challenging. Here, a simple asymmetric plasmonic molecule consisting of a central metal disk and two side-coupled parallel metal rods is demonstrated. The simulation and experimental results clearly show that double Fano resonances appear in the transmission spectrum. In addition, the two Fano peaks can be independently tuned and single/double Fano peak switching can be achieved by changing one rod length or the gap distances between the rods and the disk. The modulation method is simple and effective, which greatly increases the tunability of the structure. The proposed asymmetric artificial plasmonic molecule can have applications in multi-channel optical switches, filters and biosensors. Moreover, the controllable plasmonic field intensity in the gap between the disk and rods also provides a new control means for plasmon-induced photocatalytic reactions and biosynthesis.

Received 16th January 2020,
Accepted 18th March 2020

DOI: 10.1039/d0nr00461h

rsc.li/nanoscale

1. Introduction

Artificial plasmonic molecules are small assemblies of metallic nanoparticles. Such well-defined assemblies of particles are attracting more and more interest for sustaining localized surface plasmon resonance (LSPR) and the plasmon coupling between metallic nanoparticles. The LSPR is associated with the collective oscillation of the conductive electrons in the metal nanoparticles, which are irradiated with light at a certain wavelength.[1] The plasmon resonance mode of individual nanoparticles couples with that of the adjacent nanoparticles, forming new normal modes of the cluster. The strong interactions of resonances in plasmon molecules can be widely used for surface-enhanced spectroscopy,[2,3] nanoantennas,[4,5] biochemical sensors,[6–9] and so on. The most prominent feature of artificial plasmon molecules is the freedom to be able to design metal nanoparticles at will to achieve well-controlled optical properties which are often difficult to obtain directly from natural materials, such as Fano resonance[10–13] and analog electromagnetically induced transparency (EIT).[14–17]

There have already been many kinds of artificial plasmonic molecules based on Fano resonance, ranging from single nanodisks to dimers and multiparticle oligomers. In single nanodisk structures, Fano resonances are often generated by introducing regularly arranged defects, such as cut-out wedge,[18] narrow split gap,[19] and so on. In these structures, the nanodisk contributes to a broad superradiant dipole plasmon resonance mode (bright mode), whereas the cut-out wedge or split gap contributes to a narrow subradiant quadrupole

[a]State Key Laboratory of Advanced Design and Manufacturing for Vehicle Body, College of Mechanical and Vehicle Engineering, Hunan University, Changsha 410082, People's Republic of China. E-mail: duanhg@hnu.edu.cn
[b]School of Mathematics and Statistics, Hunan University of Technology and Business, Changsha 410205, People's Republic of China
[c]Department of Electrical and Electronic Engineering, Southern University of Science and Technology, Shenzhen518055, People's Republic of China
[d]School of Physics Science and Technology, Lingnan Normal University, Zhanjiang 524048, People's Republic of China
[e]Science and Technology on Electronic Test and Measurement Laboratory, School of Instrument and Electronics, North University of China, Taiyuan 030051, People's Republic of China

†Electronic supplementary information (ESI) available: Additional information about the polarization dependency of the Fano resonance, the surface charge distributions of the disk, the model of multimode coupled radiating oscillator theory (MCROT), and the influence of manufacture errors on optical characteristics. See DOI: 10.1039/d0nr00461h

plasmon resonance mode (dark mode). As a result, the destructive interference between the narrow subradiant mode and the broad superradiant mode produces a pronounced Fano resonance. In dimers, two closely adjacent metallic nanoparticles differing in size or shape can give rise to a remarkable Fano resonance.[20–22] Moreover, some other dual-particle structures have also been demonstrated for supporting Fano resonance, such as nanoprism pairs,[23] nanocross-bars,[24] asymmetric double bars,[25–27] ring-disks,[28,29] and concentric rings.[30] In multiparticle oligomers,[31–39] three or more particles are assembled to produce Fano resonance, which comes from the destructive interference between the bonding mode and the antibonding mode.[35,36,38,40] For a bonding mode, known as a superradiant bright mode, the dipolar plasmons of all nanoparticles oscillate in phase and in the same direction. For an antibonding mode, the dipolar moment of the center particle opposes the dipole moment of the surrounding ring, which is named a subradiant dark mode. Since multiparticle oligomers are composed of several sub-unit nanoparticles, their symmetry can be broken by changing the size and position of a single particle, which provides more degrees of freedom to manipulate the Fano resonance.[41,42] However, in plasmonic multiparticle oligomers, the bonding mode (in-phase mode) and anti-bonding mode (anti-phase mode) often come from the collective resonances of multiple particles. Therefore, the tuning effect on Fano resonance by modulating a single particle in multiparticle oligomers is often not obvious, and the modulation intensity and range of resonance modes are limited.[33,37,38,43–45] In addition, many multiparticle oligomers can only support a single Fano resonance, while multiple Fano resonances mostly occur in complex and multilayer structures,[46–48] which bring difficulties to fabrication and practical application. Therefore, designing a simpler multi-Fano resonance system to effectively tune the resonance modes is of great significance in the application of artificial plasmonic molecules.

In this paper, we propose a simple plasmonic molecule consisting of a gold disk and two side-coupled parallel gold rods. Double Fano resonances are numerically and experimentally studied, which are derived from the destructive interference between the superradiant dipole mode of the disk and the subradiant quadrupole modes of the two asymmetric rods. In addition, the structure asymmetry and the distances between the disk and rods are varied to investigate the evolution trend of the double Fano resonances. Since the two subradiant quadrupole modes are excited by the two rods respectively, single/double Fano peak(s) can be switched only by changing the length of one rod. The modulation method is simple and effective, and the modulation band is wide, which can make the two Fano peaks completely independent. Moreover, the single/double Fano peak(s) can also be switched by changing the coupling distances between the rods and the disk. The transmission modulation intensity of the Fano peaks is large, which greatly increases the tunability of the system. Lastly, we introduce a multimode coupled radiating oscillator theory (MCROT) to explain the formation mechanism of double Fano resonances. The analytical results are well verified by the finite-difference time-domain (FDTD) simulation results. The proposed asymmetric artificial plasmonic molecules can precisely tailor the transmission spectrum and make full use of it in multi-channel optical switches, filters and biosensors. In addition, by monitoring the Fano peaks and choosing an appropriate coupling distance, the plasmonic field with controllable intensity can be generated in the gap between the disk and rods, which can provide a new control method for plasmon-induced photocatalytic reactions and biosynthesis.

2. Results and discussion

Fig. 1(a) is the schematic of an individual asymmetric artificial molecule on the quartz substrate. The molecule consists of a gold disk which is side-coupled with two parallel gold rods. The specific structural parameters of the molecule are shown in Fig. 1(b). The radius (R) of the gold disk is fixed at 250 nm. The lengths of rod 1 and rod 2 are L_1 and L_2, while the widths (w) of the two rods are fixed at 50 nm. The gap distances between the disk and two rods are defined as g_1 and g_2, respectively, and the thicknesses (t) of the disk and two rods are fixed at 30 nm. Fig. 1(c) demonstrates the fabrication processes of the structure. First, a polymethyl methacrylate (PMMA) resist layer is spin coated on a quartz substrate, and then the structure is exposed to focused electron beam and developed in a developer solution. After that, chromium and gold films with thicknesses of 0.5 nm and 30 nm are deposited on the samples in turn. Finally, the gold structures are obtained by employing the liftoff process. The fabricated samples are shown in Fig. 1(d) and (e), which present an array of asymmetric artificial molecules and an enlarged randomly selective structure, respectively. The regularity and precision of the structures demonstrate that the samples can be fabricated over a large area uniformly by this method.

The transmission characteristics of the asymmetric artificial molecules are shown in Fig. 2. As a reference, the transmission characteristics of the disk independently coupled with each rod are also provided. The experimental spectra of the structures and their corresponding SEM images are shown in Fig. 2(a) and (b), respectively. The polarization direction of the light source is perpendicular to the rods, which is indicated by a black arrow in Fig. 2(b). The gap distances between the disk and rods are 30 nm ($g_1 = g_2 = 30$ nm), and the lengths of rod 1 and rod 2 are 700 nm and 900 nm ($L_1 = 700$ nm and $L_2 = 900$ nm), respectively. When the disk is only coupled with rod 1, an obvious Fano resonance peak is observed at 1530 nm (labeled FR1′), and another Fano resonance peak is found around 1730 nm (labeled FR2′) since the disk is only coupled with rod 2. Two Fano peaks (labeled as FR1 and FR2, respectively) simultaneously appear in the transmission spectrum when the disk is coupled with the two rods. Fig. 2(c) presents the simulated transmission spectra for the corresponding structures. It is apparent that the experimental results show a good qualitative agreement with the numerical predictions.

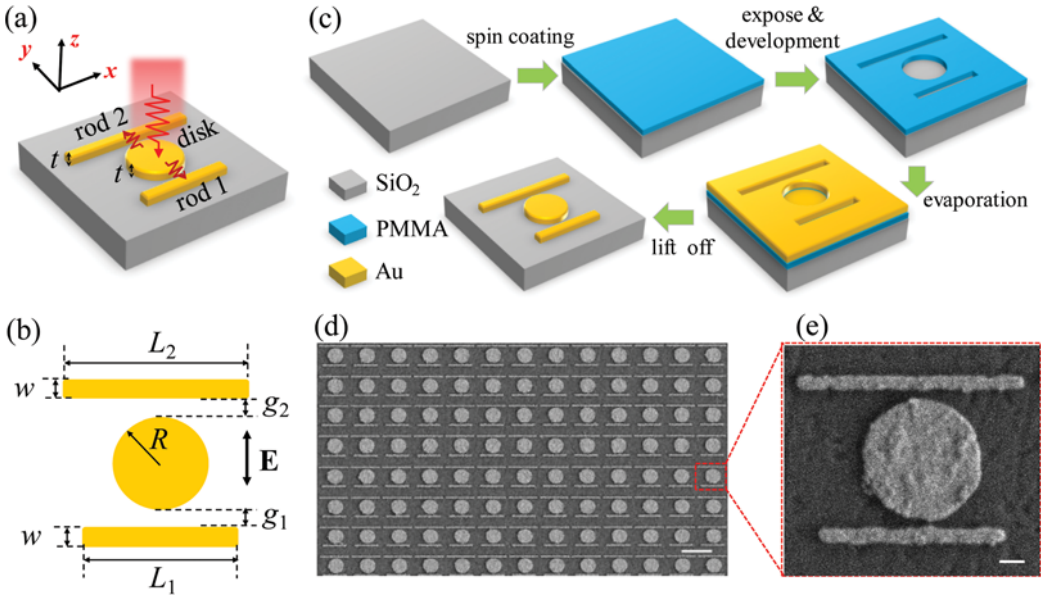

Fig. 1 Fabrication and characterization of asymmetric molecules. (a and b) Three-dimensional and two-dimensional schematic of a single asymmetric molecule, respectively. The radius R of the disk is fixed at 250 nm. The widths w of the two metal rods are fixed at 50 nm, and the lengths are L_1 and L_2, respectively. The length L_1 of the rod 1 is fixed at 700 nm. The gap distances between the disk and rod 1 and rod 2 are g_1 and g_2, respectively. The thicknesses t of the disk and rods in this study are fixed at 30 nm. (c) Schematic illustration of the fabrication flow of the asymmetric molecule. (d and e) Low- and high-magnification SEM images of a representative array of the prepared asymmetric molecular structures: (d) a randomly selected area of the array. (e) An individual structure. The scale bar dimensions in (d) and (e) are 1 μm and 100 nm, respectively.

When the polarization direction of the light source is parallel to the rods, there is no Fano resonance peak in the transmission spectra, which is confirmed in the ESI (see ESI, S1,† for the transmission spectra of the structures when the polarization direction of the light source is parallel to the rods).

To further understand the origin of the double Fano resonances in the asymmetric artificial molecule, the surface charge distributions at Fano peak spectral positions (labeled as FR1′, FR2′, FR1, and FR2 in Fig. 2(c)) are shown in Fig. 2(d). At the spectral positions FR1′ and FR2′ (the disk separately coupled with rod 1 and rod 2), the positive and negative charges form a pair of inversely arranged dipole resonances in the two metal rods, manifesting that there is almost no net dipole moment and the excitations are quadrupole plasmon resonances in the two rods. The opposite dipole moments of the quadrupole plasmon resonance lead to a narrow subradiant mode. In the disk, the distribution of surface charge at spectral position FR1′ validates that a dipole resonance is generated in the disk, and a broad superradiant mode is formed. It is noteworthy that at the spectral position FR2′, a partial positive charge distributes at the corresponding coupling position of the disk because of the Coulomb force of the negative charge in the center of the rod 2; nevertheless, the disk is still dominated by the dipole resonance mode, which is further elaborated in the ESI (see ESI, S2,† for the surface charge distributions of the disk at different spectral positions.). The formation of the distinct Fano peaks in the spectra is due to the destructive interference between the narrow subradiant quadrupole mode in the rod and the broad superradiant dipole mode in the disk. Fig. 2(d) also shows the charge distributions at spectral positions FR1 and FR2 when the disk is coupled with rod 1 and rod 2 simultaneously. At the spectral position FR1, a dipole resonance mode parallel to the polarization direction of the electric field is formed in rod 2. The interaction between the dipole resonance modes of the rod 2 and the disk is weak, so FR1 is still generated by the coupling effect between the resonance modes of the disk and rod 1, which is similar to that of FR1′. Similarly, for spectral position FR2, the Fano peak is mainly generated by the coupling effect between the resonance modes of the disk and rod 2, which is in accord with that of FR2′.

Quality factor (Q-factor) is an important parameter of Fano resonance. The Q-factor is calculated as a ratio between the resonant wavelength λ_0 and the full width at half-maximum (FWHM) $\Delta\lambda$ of a resonant peak.[49] The Q-factors of Fano resonance peaks of the proposed asymmetric artificial molecule and its decomposition structures in Fig. 2 are calculated in detail. In the decomposition structure, the Q-factors of Fano resonance peaks FR1′ and FR2′ are 13 and 7, respectively. For the coupled structure, the Q-factors of the Fano resonance peaks FR1 and FR2 are 17 and 11, respectively. Obviously, the Q-factors of Fano resonance in the asymmetric coupled structure are larger than that in the corresponding decomposition structures. The reason for this phenomenon can be attributed to the change of charge distribution on the disk. Taking FR2′ and FR2 as an example, in the decomposition structure, the disk is only coupled with rod 2 and produces Fano resonance FR2′. In the coupled structure, the disk is coupled with rod 2 and rod 1 simultaneously. The charge on rod 1 changes the charge distribution on the disk due to the Coulomb effect,

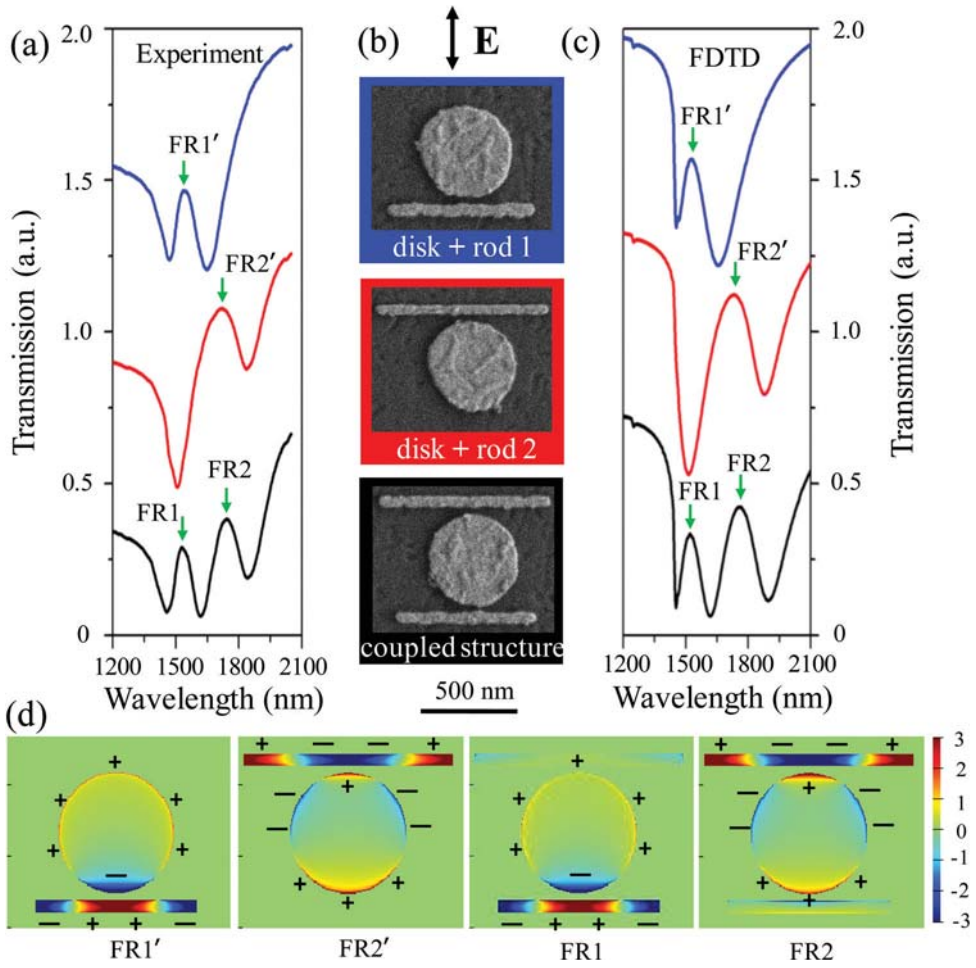

Fig. 2 Transmission characteristics of the asymmetric artificial molecule and decomposed structures. The lengths of rod 1 and rod 2 are 700 nm and 900 nm (L_1 = 700 nm and L_2 = 900 nm), respectively. (a, c) Measured (a) and FDTD simulated (c) transmittance spectra for the asymmetric artificial molecule and decomposed structures. (b) SEM images of the corresponding samples, and the black arrow represents the polarization direction of the electric field. The dimension of the scale bar at the bottom is 500 nm. (d) The surface charge distributions of the structures at FR1′, FR2′, FR1, and FR2 (λ_1 = 1530 nm, λ_2 = 1730 nm, λ_3 = 1520 nm, and λ_4 = 1760 nm).

which reduces the charge density on the disk near rod 2. Therefore, the electric field between the disk and the rod reduces, and the coupling strength between the disk and rod 2 decreases. Finally, the FWHM of FR2 decreases, and the quality factor of FR2 increases.

The optical properties of the plasmonic molecule can be understood by first starting with the highest symmetry configuration, in which the two rods are of equal length ($L_1 = L_2$ = 700 nm), and the gap distances between the disk and rods (g_1 and g_2) are fixed at 30 nm. In this case, only a single Fano peak FR1 emerges in the transmission spectrum, as shown in the top curve in Fig. 3(a). The asymmetry degree Δs of the artificial plasmonic molecule can be defined as the difference between the lengths of rod 2 and rod 1 ($\Delta s = L_2 - L_1$). As Δs increases, a split occurs at the right shoulder of FR1, and a narrow and shallow dip occurs at ~1600 nm, and then, the second Fano peak FR2 begins to appear. With the increase of Δs, the FR2 redshifts, which makes the dip between FR1 and FR2 broader and deeper. When Δs increases to 200 nm, the dip becomes broader still, but its depth now extends to the baseline, which results in two completely separated Fano peaks in the transmission spectrum. The appearance of double Fano peaks can be attributed to the shift of the resonance wavelength of rod 2. When $\Delta s = 0$ ($L_1 = L_2$), the two Fano resonances produced by the interaction of rod 1 and rod 2 with the disk are completely overlapped; therefore, only one Fano peak appears in the transmission spectrum of the system. With the increase of Δs, the resonance wavelength of rod 2 increases, and the Fano peak produced by rod 2 and the disk redshifts, while the spectral position of FR1 peaks produced by rod 1 and the disk does not change; hence, FR1 and FR2 do not completely coincide, and a split occurs at the junction of the two peaks. When Δs increases to 200 nm (L_2 = 900 nm), the two Fano peaks are completely separated. With the increase of Δs, the wavelength of FR2 shifts from 1520 nm to 1760 nm, and the modulation bandwidth reaches 240 nm. Fig. 3(c) shows the FDTD simulation results. The splitting and evolution trend of Fano peaks in the spectra are in perfect

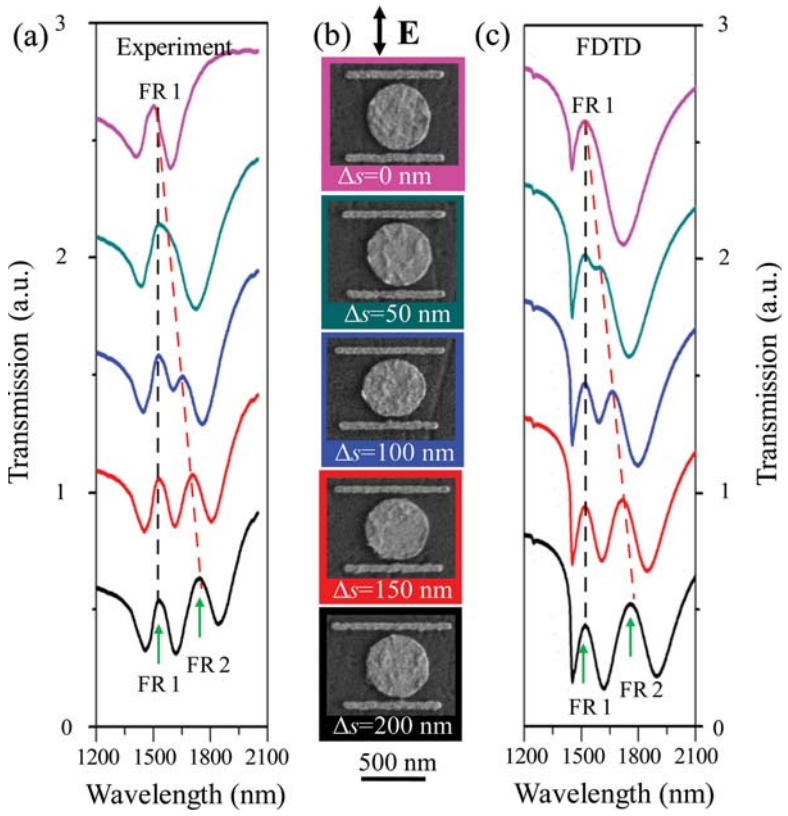

Fig. 3 Asymmetry-dependent Fano resonances. The length L_1 of rod 1 is fixed at 700 nm, and the symmetry of the structure is broken by increasing the length L_2 of rod 2. The asymmetry degree is defined as $\Delta s = L_2 - L_1$. (a and c) Measured and FDTD simulated transmission spectra for the asymmetric molecules with increasing Δs from 0 to 200 nm, respectively. (b) SEM images of the molecules with different lengths of rod 2, and the black arrow represents the polarization direction of the electric field. The dimension of the scale bar at the bottom is 500 nm.

agreement with the experimental results in Fig. 3(a). The transmission spectrum can be tailored, and single or double Fano peaks can be achieved by adjusting the asymmetry of the artificial molecule, which provides potential for application in single and double channel filters and optical switches.

We also investigate the effect of the gap distance between the disk and the rods on the optical characteristics of the asymmetric plasmonic molecule. Here, the lengths of rod 1 and rod 2 are fixed at 700 nm and 900 nm, respectively. The optical response of the asymmetric plasmonic molecule with various gap distances g_1 (g_2 is fixed to 30 nm) is studied in detail in Fig. 4. The experimental spectra of the molecules and their corresponding SEM images are shown in Fig. 4(a) and (b). With the increase of g_1, the spectral position of FR1 remains unchanged and the transmission and bandwidth decrease gradually; however, the spectral position and transmission of FR2 remain invariable. This phenomenon can be attributed to the weakening of near-field coupling between the disk and rod 1. The coupling strength between the disk and rod 1 decreases with the increase of g_1, which leads to the decrease of the transmission and bandwidth of FR1. Since the length of rod 1 is constant, the resonance wavelength of FR1 is not changed. For FR2, the gap distance g_2 between the disk and rod 2 is fixed; hence, its spectral position and transmission remain unchanged. Turning toward the molecule with a large gap distance (g_1 = 100 nm), the coupling strength between the disk and rod 1 became very weak, and the FR1 almost disappeared; the spectrum shows approximately the same behavior as the disk only coupled with rod 2 (shown in Fig. 2). Fig. 4(c) presents the simulated result for the asymmetric molecule with different g_1. It is apparent that the experimental results show a good qualitative agreement with the numerical simulations. The slight shape difference of Fano peaks between experimental and simulated results is partially due to the accuracy error of the experimental preparation. Nevertheless, all the main spectral features including the evolution trend of FR1 are clearly predicted.

The transmission characteristics of the asymmetric plasmonic molecule with different gap distances between the disk and rod 2 are also investigated. The transmission spectra of structures with various g_2 from 30 nm to 100 nm (g_1 is fixed to 30 nm) are shown in Fig. 5. Fig. 5(a) and (c) are the experimental and simulated transmission spectra of the molecules, and Fig. 5(b) is the corresponding SEM image of the structures. The evolution trend of FR2 is the same as that of FR1 in Fig. 4. With the increase of g_2, the transmission and bandwidth of FR2 decrease, which can also be attributed to the decrease of the coupling strength between the disk and rod 2. Strikingly, the peak 2 vanishes completely when g_2 reaches 100 nm, and the transmission spectrum closely resembles that

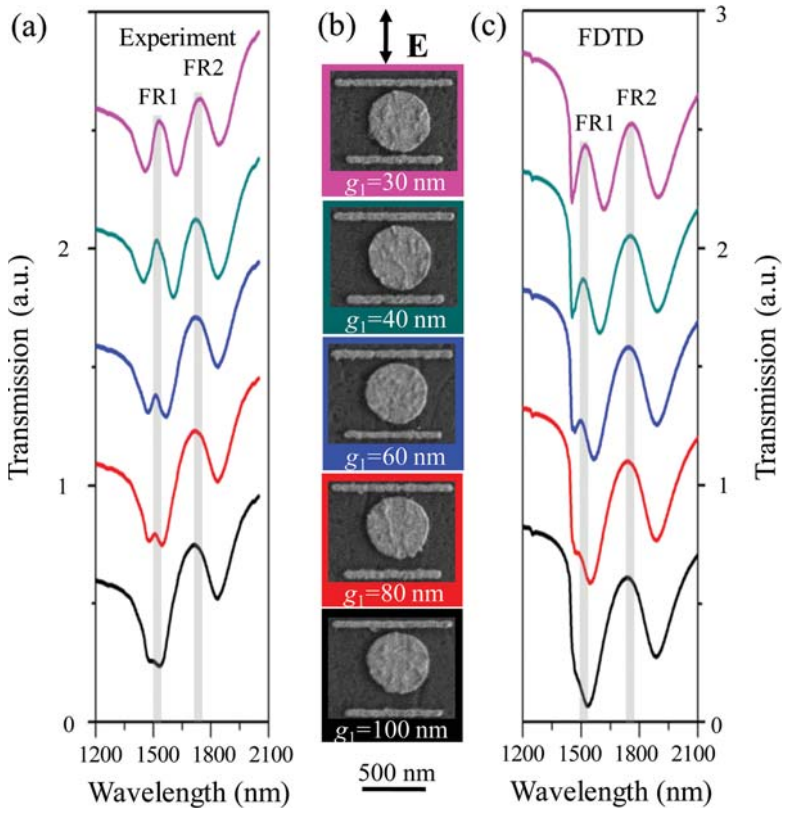

Fig. 4 Gap distance (g_1)-dependent Fano resonances. The lengths L_1 and L_2 are fixed at 700 nm and 900 nm, respectively, and the gap distance g_2 between the disk and rod 2 is fixed at 30 nm. (a) Measured and (c) FDTD simulated transmission spectra for the asymmetric artificial molecules with the gap distance g_1 increasing from 30 to 100 nm. (b) SEM images of the fabricated molecules with different gap distances g_1, and the black arrow represents the polarization direction of the electric field. The dimension of the scale bar at the bottom is 500 nm.

of the disk only coupled with rod 1 (shown in Fig. 2), indicating that the disk and rod 2 are only very weakly coupled. Hence, by changing the gap distance between the disk and rods, the transmission spectrum with single or double Fano peaks can be effectively controlled, which provides the potential for application in multi-channel filters and optical switches. In addition, recent studies have shown that the field enhancement induced by surface plasmon can influence some chemical catalysis and biomolecular synthesis.[50,51] Therefore, by monitoring the Fano peaks and selecting an appropriate coupling distance (g_1 and g_2) to enhance the plasmon field in the gaps, it can be used to effectively control the bonding/dissociation process of chemical molecules and the synthesis/decomposition process of biological molecules. These results will enable new applications in the fields of plasmon-induced photocatalysis and biosynthesis.

In order to further reveal the physical mechanism of the double Fano effect and provide a quantitative description of the transmission, we introduce a multimode coupled radiating oscillator theory (MCROT)[52] to analyze the optical characteristics of the artificial molecule. In this plasmonic molecule, there are three resonance modes, a bright mode of the disk is excited by the incident light, and two dark modes of the two rods are excited by the bright mode. By analogy with the classical harmonic oscillator model, the transmission of the coupled system can be deduced as

$$T = \left| \frac{2}{2 + \xi\sigma_{se}} \right|^2, \quad (1)$$

where ξ is the wave impedance of the external waves and σ_{se} is the surface conductivity of the electric current, which can be expressed as

$$\sigma_{se} \approx \varepsilon_0 \chi_{se}^{(static)} \frac{-i\omega a_0(\omega)}{f(\omega)} = \frac{-i\omega D_1 D_2}{D_0 D_1 D_2 - D_2 {\kappa_{01}}^2 - D_1 {\kappa_{02}}^2}, \quad (2)$$

$\varepsilon_0\chi_{se}^{(static)} = 1$ when in a vacuum, and $D_N = 1 - (\omega/\omega_N)^2 - i\gamma_N(\omega/\omega_N)$ (N = 0, 1, and 2). ω_N and γ_N are the resonance frequency and damping factor of the bright and dark modes and κ_{01} and κ_{02} are the coupling coefficients between the disk and rod 1 and rod 2 respectively, which are used to characterize the coupling strength between the disk and rods. The transmission characteristics of the asymmetric artificial molecule can be analyzed in detail by using the theoretical expressions mentioned above. (Detailed derivation can be found in the ESI, S3†.)

The evolution trends of the spectra from the two aspects of asymmetry degree and coupling distance are verified by the

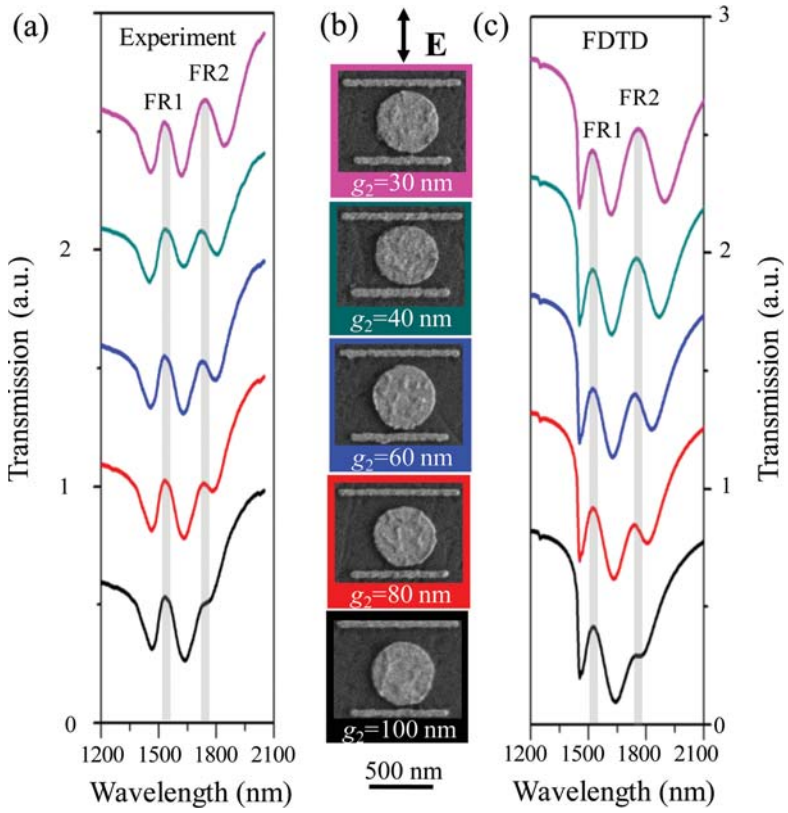

Fig. 5 Gap distance (g_2)-dependent Fano resonances. The lengths L_1 and L_2 are fixed at 700 nm and 900 nm, respectively, and the gap distance g_1 between the disk and rod 1 is fixed at 30 nm. (a) Measured and (c) FDTD simulated transmission spectra for the asymmetric artificial molecules with the gap distance g_2 increasing from 30 to 100 nm. (b) SEM images of the fabricated molecules with different gap distances g_2, and the black arrow represents the polarization direction of the electric field. The dimension of the scale bar at the bottom is 500 nm.

MCROT. The FDTD numerically simulated and theoretically calculated transmission spectra for asymmetric molecular structures are shown in Fig. 6(a). The structural parameters and asymmetry of the structure are in accordance with those in Fig. 3. The solid curves are the simulation results, and the blue circles are the theoretical fittings. The theoretical fittings vividly show the evolution trend of transmission spectra from a single Fano peak to double Fano peaks with the increase of asymmetry degree Δs, and this evolution trend is in excellent agreement with the FDTD simulations. However, there are some deviations in the fitting near the resonance peak FR1. This can be attributed to the detuning of the coupling between the disk and the two rods. With the increase of the length of rod 2, the polarization charge distribution on the disk and the spatial electric field distribution near rod 1 are changed, so the coupling coefficient κ_{01} between rod 1 and the disk is changed, making the fitting effect near FR1 not ideal. Using eqn (1), we further investigate the spectral evolution trend with different gap distances. There is a corresponding relationship between the gap distance (g_1 and g_2) and coupling coefficient (κ_{01} and κ_{02}). The coupling strength of the disk to the rod in our proposed structure can be quantitatively expressed as follows: $\kappa_{0n} = \frac{1}{8}\iiint \Delta\varepsilon_0 E_n^* \cdot E_0 \mathrm{d}x\mathrm{d}y\mathrm{d}z$ (n = 1 and 2 represent rod 1 and rod 2, respectively),[53] where E_0 and E_n are the electric fields generated by the disk and rods, respectively. The electric field distribution of the disk and rods in space is uneven, and the electric field strength is related to the coupling distance. Therefore, the coupling strength between the disk and the rod is a function of the coupling distance, and its value changes with the coupling distance. For the purpose of simplifying calculation, we use the coupling strength to express the coupling distance between the disk and the rod in MCROT fitting. Fig. 6(b) and (c) show the theoretical evolution of transmission spectra with coupling coefficients κ_{01} and κ_{02}, respectively. In Fig. 6(b), κ_{01} decreases with the increase of g_1 (κ_{02} remains unchanged), and FR1 gradually disappears while FR2 remains unchanged, which is consistent with the trend in Fig. 4(a). FR2 gradually decreases and vanishes with the decrease of κ_{02} (g_2 increases), while FR1 does not change (g_1 remains unchanged), as depicted in Fig. 6(c). The evolution trend of FR2 is also in accord with that in Fig. 5(a). So, it can be concluded that the introduced MC-ROT can provide a clear understanding of double Fano resonances in the asymmetric artificial molecule. The evolution trend of transmission spectra can be accurately predicted by quantitatively analyzing the interaction between the bright resonance mode of the disk and the dark resonance modes of the rods.

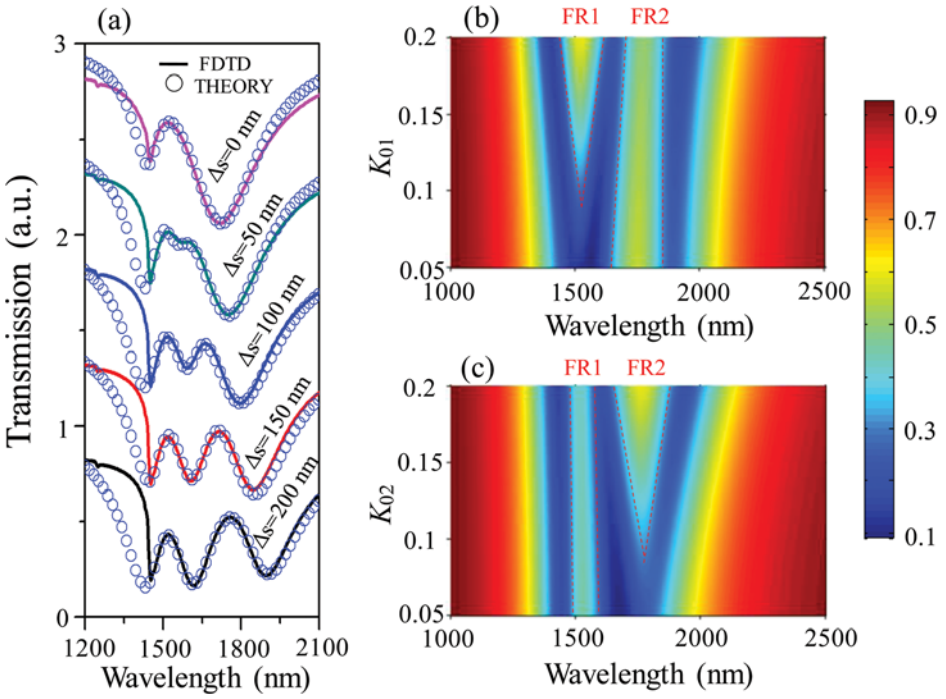

Fig. 6 Theoretical analysis of optical properties for asymmetric molecules. (a) The FDTD numerically simulated and MCROT calculated transmission spectra for structures with different degrees of asymmetry. (b) Evolution of the transmission spectra *versus* different gap distances g_1 (represented by coupling strength κ_{01} between the disk and rod 1) and wavelength (λ). (c) Evolution of the transmission spectra *versus* different gap distances g_2 (represented by coupling strength κ_{02} between the disk and rod 2) and wavelength (λ). The fitting parameters in (a) are set as follows: (L_2 = 700 nm) [κ_{01}, κ_{02}] = [0.10, 0.10], [γ_0, γ_1, γ_2] = [0.04, 0.06, 0.06]; (L_2 = 750 nm) [κ_{01}, κ_{02}] = [0.10, 0.11], [γ_0, γ_1, γ_2] = [0.04, 0.05, 0.07]; (L_2 = 800 nm) [κ_{01}, κ_{02}] = [0.10, 0.13], [γ_0, γ_1, γ_2] = [0.06, 0.06, 0.06]; (L_2 = 850 nm) [κ_{01}, κ_{02}] = [0.10, 0.15], [γ_0, γ_1, γ_2] = [0.06, 0.055, 0.06]; (L_2 = 900 nm) [κ_{01}, κ_{02}] = [0.10, 0.17], [γ_0, γ_1, γ_2] = [0.06, 0.055, 0.07].

3. Conclusion

In summary, we systematically investigated the optical characteristics of a hybrid disk/rod asymmetric artificial molecule. The transmission spectrum can be tailored by adjusting the asymmetry of the molecule. Two distinct Fano resonance peaks, which can be attributed to the destructive interference between the superradiant dipole resonance mode of the disk and the subradiant quadrupole resonance modes of the two rods, can be observed in the transmission spectrum. The two Fano peaks can be tuned independently and single/double Fano peak switching can be achieved by changing the rod length or the gap distances between the rods and the disk. The modulation method is simple and effective. Moreover, the transmission modulation intensity of the Fano peak is large, and the modulation band is wide, which greatly increases the tunability of the system. The multimode coupled radiating oscillator theory (MCROT) completely reveals the formation mechanism of double Fano resonances. The proposed artificial molecule is simple in structure and can be used for multichannel optical switches, filters and sensors in integrated chips. In addition, the controllable intensity generated in the gap between the disk and rods provides a new control approach for plasmon-induced photocatalytic reactions and biosynthesis.

4. Experimental section

Fabrication method

All samples were fabricated by using an electron-beam lithography (EBL) system (Raith 150^{two}) using PMMA resist on a quartz substrate. The substrates were rinsed in acetone and IPA for 10 min before spin coating. PMMA with a concentration of 3% was used to make the PMMA layer thinner and fabricate the structures accurately. The PMMA resist was spin coated on the quartz substrate at a speed of 3500 rpm, and the thickness of the PMMA layer is ~85 nm. To reduce the charging effect, a conductive polymer layer was spin-coated on the PMMA layer at a spin speed of 4000 rpm. After spin coating, the sample was loaded into the EBL system for exposure with 30 kV accelerating voltage. After exposure, the samples were first rinsed in deionized water to remove the conductive polymer layer and then developed in a developer (MIBK : IPA = 1 : 3) for 1 min and transferred into IPA stopper for 0.5 min. Finally, the samples were dried by N_2 flow. 30 nm gold and 0.5 nm Cr adhesion layers were deposited onto the sample with an evaporation rate of 1 Å s^{-1} with a thermal evaporator (JSD300). Liftoff was conducted in acetone and then rinsed in IPA. Finally, the gold structures were obtained after being dried by N_2 flow. There were manufacture errors in the process of EBL and metal thermal evaporation, which affect the actual

size and surface homogeneity of the samples. The simulation results show that when the manufacture errors are about 10 nm, the influence of the uneven surface and perturbation of the structure size on the optical characteristics of the artificial plasmonic molecule is very small (see ESI, S4,† for the influence of manufacture errors on optical characteristics).

FDTD simulation

The simulation of transmission spectra and charge distributions is performed by using a commercial software (FDTD solution 8.0 version, Lumerical Solution Inc.). The parameters of the samples are determined by FDTD simulation results. Corresponding to the measured spectrum from the structure array, the periodic boundary conditions are set in *X* and *Y* axes and a perfect-matched layer is used in the *Z* axis. The spatial step of the discrete mesh in the simulation is set to be 5 nm in the *XY* plane and 2 nm in the *Z* direction. The complex dielectric constants for Au and SiO_2 were selected from the Palik database.

Optical measurement

To investigate the optical characteristics of the artificial plasmonic molecules, the transmission spectrum measurement is performed in the transmittance mode using a 20/30PV UV-visible-NIR range micro-spectrometer (CRAIC Technology Inc.). In measurement, the light from a Xeon bubble through a stand Kohler lens was incident on the sample with normal incident. The transmitted signal is first collected by using an objective (17×, N.A. = 0.25), screened using an aperture to exclude the angular transmitted light and detected using a CCD camera. A polarizer is inserted in the incident path for linear excitation in the spectral range of interest. The polarization direction of the incident light is perpendicular to the long axis of the gold rods. The integration time is set to 140 ms.

Conflicts of interest

There are no conflicts to declare.

Acknowledgements

We gratefully acknowledge financial support from the National Natural Science Foundation of China (Grant No. 11574078, 51722503 and 51621004).

References

1 W. L. Barnes, A. Dereux and T. W. Ebbesen, *Nature*, 2003, **424**, 824–830.
2 H. Wang, J. Kundu and N. J. Halas, *Angew. Chem., Int. Ed.*, 2007, **46**, 9040–9044.
3 T. Wang, Z. Dong, E. H. H. Koay and J. K. W. Yang, *ACS Photonics*, 2019, **6**, 1272–1278.
4 V. Giannini, A. I. Fernández-Domínguez, S. C. Heck and S. A. Maier, *Chem. Rev.*, 2011, **111**, 3888–3912.
5 N. Xingjie, N. K. Emani, A. V. Kildishev, B. Alexandra and V. M. Shalaev, *Science*, 2012, **335**, 427.
6 C. Caucheteur, T. Guo and J. Albert, *Anal. Bioanal. Chem.*, 2015, **407**, 3883–3897.
7 M. Sriram, K. Zong, S. R. C. Vivekchand and J. J. Gooding, *Sensors*, 2015, **15**, 25774–25792.
8 Z. Chen, P. Li, S. Zhang, Y. Chen, P. Liu and H. Duan, *Nanotechnology*, 2019, **30**, 335201.
9 S. Zhan, J. Xiong, G. Nie, S. Wu, J. Hu, X. Wu, S. Hu, J. Zhang, Y. Gao and Y. Liu, *Adv. Mater. Interfaces*, 2019, **6**, 1802089.
10 A. Lovera, B. Gallinet, P. Nordlander and O. J. F. Martin, *ACS Nano*, 2013, **7**, 4527–4536.
11 B. Luk'yanchuk, N. I. Zheludev, S. A. Maier, N. J. Halas, P. Nordlander, H. Giessen and C. T. Chong, *Nat. Mater.*, 2010, **9**, 707–715.
12 G. Li, H. Hu and L. Wu, *Phys. Chem. Chem. Phys.*, 2019, **21**, 252–259.
13 J. Chen, F. Gan, Y. Wang and G. Li, *Adv. Opt. Mater.*, 2018, **6**, 1701152.
14 R. Taubert, M. Hentschel, J. Kästel and H. Giessen, *Nano Lett.*, 2012, **12**, 1367–1371.
15 X. Niu, X. Hu, Q. Yan, J. Zhu, H. Cheng, Y. Huang, C. Lu, Y. Fu and Q. Gong, *Nanophotonics*, 2019, **8**, 1125.
16 Z. Li, Y. Ma, R. Huang, R. Singh, J. Gu, Z. Tian, J. Han and W. Zhang, *Opt. Express*, 2011, **19**, 8912–8919.
17 H. Xu, Y. Lu, Y. Lee and B. Ham, *Opt. Express*, 2010, **18**, 17736–17747.
18 Z. Fang, J. Cai, Z. Yan, P. Nordlander, N. J. Halas and X. Zhu, *Nano Lett.*, 2011, **11**, 4475–4479.
19 S. Zhang, G. C. Li, Y. Chen, X. Zhu, S. D. Liu, D. Y. Lei and H. Duan, *ACS Nano*, 2016, **10**, 11105–11114.
20 L. V. Brown, H. Sobhani, J. B. Lassiter, P. Nordlander and N. J. Halas, *ACS Nano*, 2010, **4**, 819–832.
21 W. Lu, X. Cui, T. H. Chow, L. Shao, H. Wang, H. Chen and J. Wang, *Nanoscale*, 2019, **11**, 9641–9653.
22 F. Qin, Y. Lai, J. Yang, X. Cui, H. Ma, J. Wang and H. Q. Lin, *Nanoscale*, 2017, **9**, 13222–13234.
23 H. Duan, A. I. Fernández-Domínguez, M. Bosman, S. A. Maier and J. K. W. Yang, *Nano Lett.*, 2012, **12**, 1683–1689.
24 N. Verellen, P. Van Dorpe, C. Huang, K. Lodewijks, G. A. E. Vandenbosch, L. Lagae and V. V. Moshchalkov, *Nano Lett.*, 2011, **11**, 391–397.
25 Z. Yang, Z. Zhang, L. Zhang, Q. Li, Z. Hao and Q. Wang, *Opt. Lett.*, 2011, **36**, 1542–1544.
26 Y. Moritake, Y. Kanamori and K. Hane, *Opt. Lett.*, 2014, **39**, 4057–4060.
27 Y. Moritake, Y. Kanamori and K. Hane, *Opt. Express*, 2016, **24**, 9332–9339.
28 Y. Fu, J. Zhang, Y. Yu and B. Luk'yanchuk, *ACS Nano*, 2012, **6**, 5130–5137.
29 F. Hao, P. Nordlander, M. T. Burnett and S. A. Maier, *Phys. Rev. B: Condens. Matter Mater. Phys.*, 2007, **76**, 245417.

30 J. Shu, W. Gao and Q. Xu, *Opt. Express*, 2013, **21**, 11101–11106.
31 L. Chuntonov and G. Haran, *Nano Lett.*, 2011, **11**, 2440–2445.
32 J. A. Fan, K. Bao, C. Wu, J. Bao, R. Bardhan, N. J. Halas, V. N. Manoharan, G. Shvets, P. Nordlander and F. Capasso, *Nano Lett.*, 2010, **10**, 4680–4685.
33 J. B. Lassiter, H. Sobhani, J. A. Fan, J. Kundu, F. Capasso, P. Nordlander and N. J. Halas, *Nano Lett.*, 2010, **10**, 3184–3189.
34 S. Zu, Y. Bao and Z. Fang, *Nanoscale*, 2016, **8**, 3900–3905.
35 J. B. Lassiter, H. Sobhani, M. W. Knight, W. S. Mielczarek, P. Nordlander and N. J. Halas, *Nano Lett.*, 2012, **12**, 1058–1062.
36 W. S. Chang, J. B. Lassiter, P. Swanglap, H. Sobhani, S. Khatua, P. Nordlander, N. J. Halas and S. Link, *Nano Lett.*, 2012, **12**, 4977–4982.
37 J. Ye, F. Wen, H. Sobhani, J. B. Lassiter, P. Van Dorpe, P. Nordlander and N. J. Halas, *Nano Lett.*, 2012, **12**, 1660–1667.
38 M. Hentschel, D. Dregely, R. Vogelgesang, H. Giessen and N. Liu, *ACS Nano*, 2011, **5**, 2042–2050.
39 D. Dregely, M. Hentschel and H. Giessen, *ACS Nano*, 2011, **5**, 8202–8211.
40 M. Hentschel, M. Saliba, R. Vogelgesang, H. Giessen, A. P. Alivisatos and N. Liu, *Nano Lett.*, 2010, **10**, 2721–2726.
41 L. Chuntonov and G. Haran, *J. Phys. Chem. C*, 2011, **115**, 19488–19495.
42 T. K. Nguyen, T. D. Le, P. T. Dang and K. Q. Le, *J. Opt. Soc. Am. B*, 2017, **34**, 668.
43 H. Hu, F. Zhang, G. Li, J. Chen, Q. Li and L. Wu, *Photonics Res.*, 2018, **6**, 204–213.
44 S. Lepeshov, A. Krasnok, I. Mukhin, D. Zuev, A. Gudovskikh, V. Milichko, P. Belov and A. Miroshnichenko, *ACS Photonics*, 2017, **4**, 536–543.
45 Z. He, J. Zhao and H. Lu, *Appl. Phys. Express*, 2020, **13**, 012009.
46 S. Liu, Z. Yang, R. Liu and X. Li, *ACS Nano*, 2012, **6**, 6260–6271.
47 N. Liu, M. Hentschel, T. Weiss, A. P. Alivisatos and H. Giessen, *Science*, 2011, **332**, 1407–1410.
48 A. Artar, A. A. Yanik and H. Altug, *Nano Lett.*, 2011, **11**, 1685–1689.
49 Y. Zhang, W. Liu, Z. Li, Z. Li, H. Cheng, S. Chen and J. Tian, *Opt. Lett.*, 2018, **43**, 1842–1845.
50 E. Kazuma, J. Jung, H. Ueba, M. Trenary and Y. Kim, *Science*, 2018, **360**, 521.
51 G. Haran and L. Chuntonov, *Chem. Rev.*, 2018, **118**, 5539–5580.
52 Z. Chen, H. Li, S. Zhan, B. Li, Z. He, H. Xu and M. Zheng, *Sci. Rep.*, 2016, **6**, 24446.
53 F. Yang, Y. Liu and L. You, *Phys. Rev. A*, 2017, **96**, 053845.